# Development of a TES for Antenna-Coupled Bolometer for Cosmic Microwave Background Detection

Edvige Celasco, Lorenzo Ferrari Barusso, Matteo De Gerone, Giovanni Gallucci, Daniele Grosso, Pietro Manfrinetti, Luca Repetto, Marine Schott, and Flavio Gatti

***Abstract*—In the most recent development in cosmic microwave detection, there is great interest for planar antenna coupled transition edge sensor (TES), which allows performance that meets the requirements of future cosmology mission. In particular, we are developing such kinds of bolometers with a planar sinuous antenna that are well suited for dense arrays for both imaging and polarization measurement, for cosmic mircowave background (CMB), earth observation, and security. In this article, we are selecting two different TES platform (Ti/Au and Ir/Au) options suitable for high-performance bolometer to be operated in space applications. We present here a preliminary bolometer design and first studies for the realization of Ti/Au and Ir/Au TESs, with particular regard to the dependence of the transition temperature $T_c$ on the thermal profile and oxygen contamination during the production or annealing process.**

***Index Terms*—Bolometer, sensor, superconductivity.**

## I. Introduction

As part of the advancement of inflationary cosmology experiments, large planar arrays of multichroic, polarization-sensitive transition edge sensor (TES) bolometers coupled to broadband antennas have been proposed and are being developed for the focal plane of CMB telescopes [1] (works on antenna coupled bolometers).

As part of these developments, we are leading a national project funded by the Italian Space Agency to build high-sensitivity bolometers coupled to sinuous planar antenna for future stratospheric balloon missions or ground-based telescopes. The project is in a start-up phase, and we are focusing our attention on the selection of TES sensors for the bolometer. In this work, we compare already developed TES platforms, Ir/Au on Si(100 oriented) and Ti/Au on $Si_3N_4$ substrate, 1.5 $\mu$m thick, that is deposited onto a silicon wafer (100 oriented) coated with a 0.3 $\mu$m $SiO_2$ thermal layer, which can provide high responsivity and intrinsic power spectral density in the $aWs^{1/2}$ region, but also long-term performance stability and compatibility with detector fabrication processes.

The motivation for these two platforms is related to the experience accumulated by the research group over the years. Titanium/Au has the advantage of being easier to fabricate, but needs a proximity factor, i.e., $T_c$ reduction, between 4 and 6 to work in the 100 mK region, whereas iridium has more difficulty in fabrication, but needs a proximity factor on the order of 1 or 2. This makes it easier to achieve the required reproducibility of the detector's working temperature.

Both platforms have been developed for many years as sensors for calorimeters and bolometers in the neutrino mass determination experiments, HOLMES [2] for the future X-ray telescope ATHENA [3] and in the CMB microwave telescope LSPE [4].

Both have shown excellent performance in various prototypes. On the other hand, the increasing complexity of the fabrication process has highlighted some limitations (or disadvantages) of both systems, particularly the dependence of the transition temperature $T_c$ of TES and its oxidation on the conditions under which the fabrication processes take place.

In particular, for the Ti/Au system, we observed the $T_c$ drift related to the effective temperature profile during the fabrication process, and in the Ir/Au system, the transition quality depends on an unexpected excess oxidation after the oxygen plasma step.

Here, we will briefly review the Ti/Au system and discuss the Ir/Au system in more detail based on the new experimental results.

## II. Ti/Au Platform

The Ti/Au platform had already been studied in past years regarding its suitability for a complex fabrication process of low-temperature detectors and electronics [5].

The main problem we encountered was the unexpected final $T_c$ after fabrication of the whole device in which Ti and Ti/Au are one of many components.

Manuscript received 15 July 2022; revised 12 October 2022; accepted 14 October 2022. Date of publication 20 October 2022; date of current version 29 November 2022. This work was supported in part by the Ministry of University and Research and in part by INFN within the LSPE Project and Italian Space Agency Within the Project "TES Antenna Coupled" 2020-25-HH.0. This article was recommended by Associate Editor C. Barone. *(Corresponding author: Edvige Celasco.)*

Edvige Celasco, Lorenzo Ferrari Barusso, Daniele Grosso, and Flavio Gatti are with the Dipartimento di Fisica, Università Degli Studi di Genova, 16146 Genova, Italy, and also with Istituto Nazionale Fisica Nucleare – Sezione di Genova, 16146 Genova, Italy (e-mail: celasco@fisica.unige.it; lorenzo.ferrari@ge.infn.it; grosso@fisica.unige.it; flavio.gatti@ge.infn.it).

Matteo De Gerone and Giovanni Gallucci are with Istituto Nazionale Fisica Nucleare – Sezione di Genova, 16146 Genova, Italy (e-mail: matteo.degerone@ge.infn.it; giovanni.gallucci@ge.infn.it).

Pietro Manfrinetti is with Dipartimento di Chimica, Università Degli Studi di Genova, 16146 Genova, Italy (e-mail: pietro.rareearth@hotmail.it).

Luca Repetto and Marine Schott are with Dipartimento di Fisica, Università Degli Studi di Genova, 16146 Genova, Italy (e-mail: luca.repetto@unige.it; marine.schott@edu.unige.it).

Color versions of one or more figures in this article are available at https://doi.org/10.1109/TASC.2022.3215894.

Digital Object Identifier 10.1109/TASC.2022.3215894

In other words, although the fabrication of the blank film had a $T_c$ as required and reproducible, we found an unpredictable drift of the $T_c$ toward a lower temperature after the other fabrication steps were performed.

We knew that different groups find a wide range in the $T_c$ values of Ti films (from 350 to 800 mK), and in our preliminary investigations, we found an increase in $T_c$ with samples grown on a substrate at near room temperature. In addition, we found that the temperature profile of the substrate during film growth or at any subsequent fabrication step affects the final $T_c$ of titanium. Based on this observation, we tried to reproduce by controlled annealing of Ti films the possible heats experienced during detector fabrication, finding an empirical law between the total annealing energy and the relative $T_c$.

We performed investigations to highlight the causes of this behavior: mainly focusing on possible impurity contamination and morphological structure.

We could easily rule out both contamination and morphological changes, as was reported in [5]. Atomic force microscopy confirmed reproducible grain size at different annealing temperatures, linked to the compatible roughness of all the films analyzed.

This was also confirmed with X-ray diffraction. With this double confirmation of the absence of an obvious trend in grain size variation with increasing temperature, we can conclude that no morphological variation occurs.

Another possible reason for the variation in $T_c$ could be a stress in the lattice. We had a probable clue with a shift in the XRD peak of the annealed titanium film at different temperatures. The detected shift could be related to lattice stress due to annealing temperature, but this hypothesis is still under study.

## III. Ir/Au Platform

Our interest in the Ir and Ir/Au system is based on the consideration that Ir is one of the most chemically stable materials [6] and therefore suitable for high-performance TES devices for space applications where long-term stability (on the order of 5/10 years) is required [3].

Based on the known data on chemical stability, we conclude that none of the processes used to produce Ir's TES sensors can chemically alter the film.

However, we found deeply oxidized films: This is a serious problem because iridium forms nonsuperconducting metal oxides [7] such as $IrO_2$.

It is known that at room temperature native oxidation affects a few nanometers and is a process self-limited by passivation.

On the other hand, it is also known that deep oxidations occur in an oxygen atmosphere at temperatures above 600° [6], [8]. Our iridium films were grown and processed at temperatures between room temperature and about 100 °C.

In fact, we grow the Ir films without heating the substrate, by means of a pulsed laser deposition system, based on a Q-switched NdYAG laser with an average power of 5 W, wavelength of 1064 nm, pulsewidth of 10 ns, and repetition rate of 10 Hz. The iridium ionized plume hitting the substrate, during the deposition process under ultrahigh vacuum (base pressure typically $<3 \times 10^{-9}$ mbar), causes a small local increase of temperature of the substrate, which we evaluated smaller than 100 °C. Similarly, the top gold layer was grown slowly by electron beam deposition in a subsequent deposition without vacuum breaking.

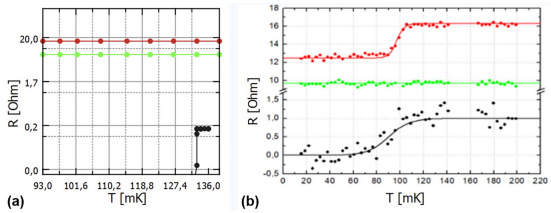


Fig. 1. Resistance versus temperature of two different samples. (a) Superconductivity behavior disappears after the first processed step (top curve, increasing the $R$ value). (b) Superconductive transition still occurs, after the first plasma oxygen step, but at higher $R$, and disappears after the second plasma oxygen treatment.

The chosen lithographic process is positive because iridium superconductivity is very sensitive to the contamination from other elements. Negative lithography was tested in the early stages of our work with negative results because we observed a suppression of superconductivity. We have also verified that the cause was due to the interaction between Ir plasma and resist polymer, whose elements were found in the film as confirmed by X-ray photoelectron spectroscopy (XPS) analyses.

Although the process temperature profile remains well below the threshold for deep oxidation, the processed detectors show problems that could be related to the formation of higher resistivity iridium oxide: such as the increase in normal resistance (3-fold to 10-fold increase), the reduction of $T_c$ with the broadening of the superconducting transition to tens of mK (increase in residual resistivity below $T_c$), and, in some cases, the complete disappearance of superconductivity.

An example of this behavior is done in Fig. 1 in which are shown the $R$ versus $T$ of two different iridium film samples, just after the growth process (bottom curve, in panels a and b), after the first processed step, including oxygen plasma (top curve) and after the second process step oxygen plasma for deep etching (middle curve).

In Fig. 1(a), an increase of the $R$ value and a suppression of the transition of the film after the first plasma oxygen step (top curve) are evident. In Fig. 1(b), the $R$ value has the same behavior, but $T_c$ still occurs.

In the middle curves of both panels a and b, the superconductive transition is completely suppressed after the second step of plasma oxygen.

In contrast, our original unprocessed Ir and Ir/Au films showed a narrow transition (1 mK) and a reproducible and stable $T_c$, as expected. This problem is less evident in the thicker films. In the latter case, $T_c$ does not seem to be affected by the process.

In order to identify the main contributors to oxidation in our manufacturing process, we analyzed the manufacturing steps that can contaminate the films to such an extent as to suppress superconductivity: lithography, etching, and cleaning.

In the last two steps, oxygen plasma is often used to adjust etching and to clean off polymeric debris.

TABLE I
CRITICAL TEMPERATURE ($T_c$), TRANSITION WIDTH $\Delta T_c$, RESIDUAL RESISTANCE RATIO FROM 300 TO 42 K RATIO (RRR), BEFORE AND AFTER PROCESS OF MAIN SAMPLES

| Name | Nominal thickness (nm) | $T_c$ (mK) | $\Delta T_c$ | $T_c$ after process (mK) | $\Delta T_c$ | RRR | RRR After etching | Process |
|---|---|---|---|---|---|---|---|---|
| Sample 1 | Ir: 105 Au: 14 | 110 | 2 | no | no | 2,4 | 2,3 | oxygen plasma and Strong ICP |
| Sample 2 | Ir: 98 Au:14 | 95,6 | 10 | no | no | 2.0 | 1,5 | oxygen plasma and Strong ICP |
| Sample 3 | Ir: 65 Au: 14 | 90 | 1 | 111 | 5 | 2,6 | 2,3 | oxygen plasma and low ICP |
| Sample 4 | Ir: 92 Au: 14 | 100 | 4 | 100 | 10 | 1,5 | 2,6 | No oxygen plasma and low ICP |
| Sample 5 | Ir: 130 Au: 14 | 162 | 4 | 160 | 4 | 1,9 | 1,82 | No oxygen plasma, Thick film, and low ICP |

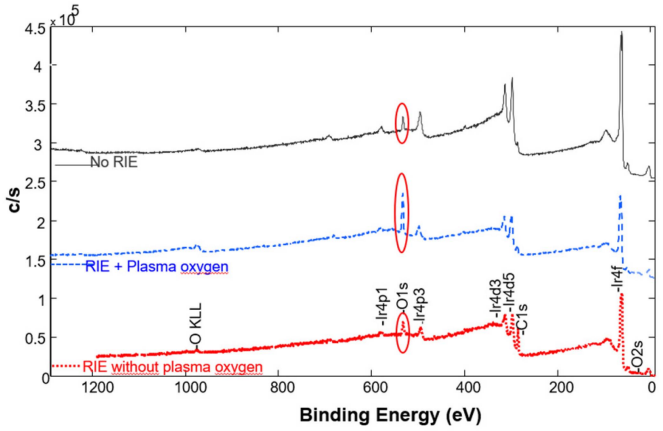


Fig. 2. XPS survey scan of bare film (continuous top spectrum), processed film with RIE and plasma oxygen (dashed central spectrum), and film after only reactive ion etching (RIE) (dotted bottom spectrum).

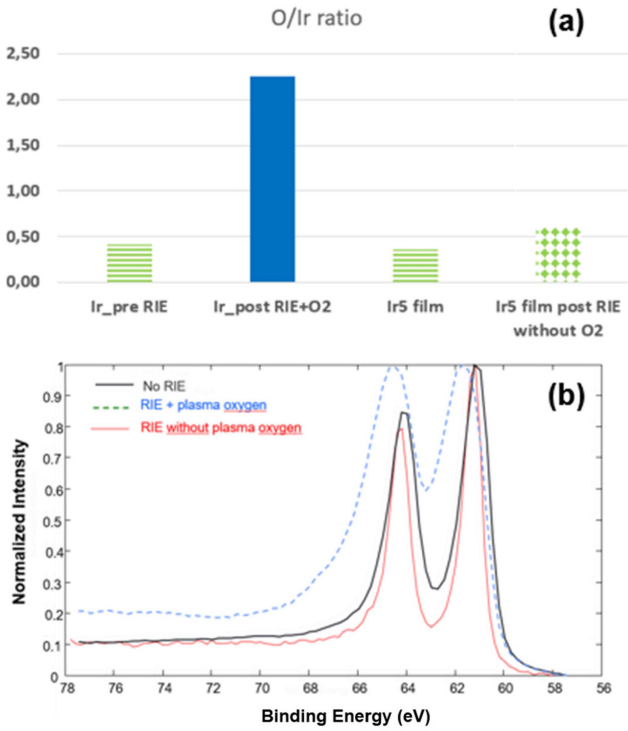


Fig. 3. (a) Histogram of atomic percentage O/Ir ratio of film before (dashed columns) and after (filled second column) RIE+plasma oxygen and before (dashed column) and after only RIE process (dotted column). (b) High resolution on iridium 4f with the typical core level shift of iridium oxide after RIE+plasma oxygen step (dashed spectrum).

In order to understand the origin of the problem, we treated several film samples as follows: each Ir film sample was grown on a <100> silicon substrate of about 15 × 15 mm, then cut into several pieces, each of which was subjected to the various manufacturing processes.

The results are presented in Table I in which a selection of representative samples is shown.

Table I shows $T_c$, $\Delta T_c$, RRR, before and after four different process sequences. It can be seen that the thinner films, highly exposed to oxygen plasma, do not exhibit a superconducting transition, in all cases immediately after exposure and plasma.

The unexposed and thicker films have good $T_c$ and negligible differences from the untreated ones.

We can conclude that oxygen plasma is the most likely cause of partial or total suppression of superconductivity.

To support this hypothesis, we analyzed the processed samples by taking the corresponding unprocessed ones as reference.

The XPS was performed by a Physical Electronics system, with an Al-K$\alpha$ monochromatic source ($\lambda = 1486.6$ eV). The spectra were plotted with a dedicated MultiPak software. The XPS analysis (see Fig. 2), although sensitive to depths of about 10 nm, clearly shows the presence of oxygen and carbon peaks and not additional peaks due to additional contamination before and after the processes. The carbon peak is due to carboxylic carbon, which is always present when the sample remains in the atmosphere.

The untreated reference sample, which has the upper XPS spectrum of Fig. 3, gives us a clear and reproducible idea of the typical amount of oxygen present in the iridium film, i.e., the so-called "native" oxygen that naturally develops whenever the film remains in the atmosphere.

The second spectrum shows a huge amount of oxygen ($O_{1s}$) after RIE and oxygen plasma processes, whereas in the third spectrum, after RIE without oxygen plasma, $O_{1s}$ line is almost unchanged.

We measure that samples undergoing oxygen plasma have four times higher $O_{1s}/Ir_{4f}$ ratio than samples treated without oxygen plasma [see Fig. 3(a)].

Even more significant is the chemical shift of iridium $Ir_{(4f)}$ showing the formation of the compound $IrO_2$ on the plasma-oxidized sample [see high-resolution scan in Fig. 3(b)]. In more detail, this panel shows all three iridium signals together to better highlight the shift of the dashed line, toward a higher binding energy. This shift corresponds to the signal of the iridium oxide and is clearly recognizable from the signal of the metallic Ir of "no RIE" and "RIE without plasma oxygen" samples.

The XPS lines of Ir films subjected to $O_2$ plasma are observed at the binding energy around 62 eV (dashed blue line) in the Ir 4f spectrum. From the position of the peak, it can be confirmed that $IrO_2$ is produced, as it has been reported that Ir 4f7/2 of $IrO_2$ (obtained by oxidation by high-temperature annealing in

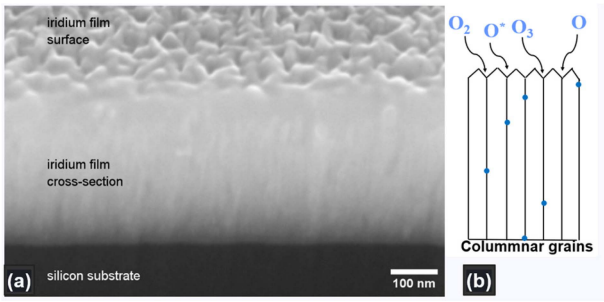


Fig. 4. (a) Iridium film on silicon: SEM image of the cross section obtained by FIB milling. A columnar structure can be observed in the central area of the image, corresponding to the sectional view of the film. The SEM image was acquired at 20 kV with an in-lens detector. (b) Schematization of possible columnar growth described in [9].

an oxygen atmosphere) appeared at 62.0¬63.7 eV, whereas Ir 4f7/2 of metallic Ir appeared at 60.6–61.0 eV [10], [11].

The observation that the XPS lines of the raw Ir film and the etched film without plasma $O_2$ (the continuous curve dark and red, respectively) are at 61 eV, as expected for metals, completes the demonstration that plasma $O_2$ is the cause of the problem of nonrepeatable TES performance. But the disappearance of iridium superconductivity must involve the bulk of the film and not only the surface.

The structure of the film was analyzed to provide a possible explanation to an oxidation deeper than the already mentioned native oxide layer. To this purpose, cross sections were obtained by ion milling in a focused ion beam-scanning electron microscopy (FIB-SEM) system (CrossBeam 1540XB, Carl Zeiss AG, Oberkochen, Germany). Fig. 4 shows an SEM image of one of these cross sections.

The SEM image shows that the iridium film has a columnar structure roughly perpendicular to the film interfaces. This kind of structure, where the sides of the columns correspond to grain boundaries, is known to favor diffusion into the film [11], [12].

A possible explanation of why an oxygen-plasma treatment can induce a deeper oxidation of the film is because energetic $O$ species, present in the plasma and impinging the film surface, can penetrate the usually passivating layer and find preferential paths into the film depth.

To corroborate the results of XPS scans, Raman spectroscopy was also performed. The spectra were recorded using an NRS-4100 Raman Microspectrometer (JASCO Co., Tokyo, Japan), with a laser source at 532 nm and a grating with 1800 lines/mm.

The Raman spectra are shown in Fig. 5. They were truncated to focus on the zone of interest $200-1150\,\mathrm{cm}^{-1}$, which corresponds to the range of vibration of the majority of $IrO_x$ compounds [14].

From these spectra, a background was removed by fitting and subtracting a polynomial of degree 4 to every spectrum. Peak positions were identified by a fitting procedure using Voigt profiles, combining both Gaussian and Lorentzian lines, to evidence the vibration frequencies for both films: the one that did not undergo $O_2$ plasma and for the one that did.

The main peak positions that were found are reported in Table II.

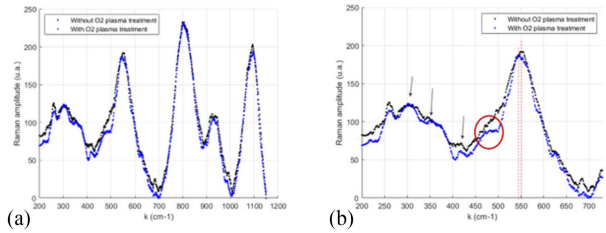


Fig. 5. Raman spectra of the two probed films for the region of interest. (a) On the full zone of interest. (b) Zoom on the zone was the fitting process performed, highlighting the main peak corresponding to the $E_g$ vibration mode of the $IrO_2$ crystalline structure and other distinctive peaks.

TABLE II
RAMAN SHIFT FOR BOTH PLASMA-PROCESSED AND NOT PLASMA-PROCESSED FILM SHOWING THE MAIN PEAK DEDUCED FROM THE FITTING PROCEDURE

| Sample | Raman shift ($cm^{-1}$) | | | |
|---|---|---|---|---|
| RIE + $O_2$ processed film | 347.47 | 421.10 | 469.49 | 551.05 |
| RIE without $O_2$ processed film | 343.49 | 431.21 | 481.30 | 557.66 |

One of the most intense peaks was observed around $550\,\mathrm{cm}^{-1}$ for both films. This Raman shift can be ascribed to the vibration of the $E_g$ mode of the rutile structure of $IrO_2$, expected at $561\,\mathrm{cm}^{-1}$. This position can be found shifted depending on the effective crystal structure and on the substrate the film was grown on [15]. Also in the literature, this peak is generally considered as the one with the highest intensity among the main three corresponding to $IrO_2$ single crystal (the others being located around 728 and $752\,\mathrm{cm}^{-1}$ for $B_{2g}$ and $A_{1g}$ vibration modes) [15], [16].

Besides this main peak, we could also notice some distinctive peaks around $350\,\mathrm{cm}^{-1}$ and $420-470\,\mathrm{cm}^{-1}$, which in previous studies [17] were ascribed to some single and double $Ir-O$ bonds of amorphous forms.

This analysis, based on the most robust features of the acquired Raman spectra, provides a picture consistent with our XPS measurements on iridium native oxide by giving an additional indication of the kind of oxidation.

Finer details that could distinguish between the two films need to be confirmed with further measurements. We however notice that the two spectra differ in the $470\,\mathrm{cm}^{-1}$ band in a feature [red circle in Fig. 5(b)] that we could not ascribe to any measurement artifact. The fact that this peak can appear because of an increased disorder in the crystal structure and because of a modification of the stoichiometry of the oxide layer can be taken as a suggestion of the modification produced by the plasma treatment.

Raman measurement confirms the presence of the iridium native oxide and its difference in the oxidation bulk due to the disorder arised after plasma oxygen.

When it occurs, the oxygen interdiffusion is facilitated by the columnar growth of the iridium films observed with field emission scanning electron microscopy (FESEM).

This observation could be of particular interest for the production of iridium oxide for catalytic applications, as recently studied in references aimed at studying the production of hydrogen currently produced in high-temperature reactors [18].

This unexpected oxidation process, by plasma oxygen, is more efficient and at room temperature than the oxidation systems studied so far.

## IV. Conclusion

The author concludes that iridium oxide is produced very efficiently both superficially and deeply in the oxygen plasma, which is characterized by the presence of $O_2$ molecules, oxygen radicals, monoatomic and ionized oxygen $O_3$. The resistivities of the oxidized films approach those of iridium oxide.

## Acknowledgment

The authors would like to thank M. Rigano, University of Genova, and L. Parodi, A. Bevilacqua, and F. Siccardi of INFN of Genova for the technical support.

## References

[1] B. Westbrook et al., "Detector fabrication development for the LiteBIRD satellite mission," *Proc. SPIE*, vol. 11443, 2020, Art. no. 114435Q, doi: 10.1117/12.2562978.

[2] B. Alpert et al., "HOLMES: The electron capture decay of 163Ho to measure the electron neutrino mass with sub-eV sensitivity," *Eur. Phys. J. C*, vol. 75, no. 3, 2014, Art. no. 1112015.

[3] D. Barret et al., "The ATHENA X-ray integral field unit (X-IFU)," *Proc. SPIE*, vol. 10699, 2018, Art. no. 106991G, doi: 10.1117/12.2312409.

[4] G. Addamo et al., "The large scale polarization explorer (LSPE) for CMB measurements: Performance forecast," *J. Cosmol. Astropart. Phys.*, vol. 2021, no. 8, 2021, Art. no. 008, doi: 10.1088/1475-7516/2021/08/008.

[5] B. Siri et al., "Impact of annealing on $T_C$ and structure of titanium thin films," *IEEE Trans. Appl. Supercond.*, vol. 31, no. 5, Aug. 2021, Art. no. 7500304.

[6] I. L. Shabalin, *Ultra-High Temperature Materials I*. New York, NY, USA: Springer, 2014.

[7] M. A. El Khakani, M. Chaker, and E. Gat, "Pulsed laser deposition of highly conductive iridium oxide thin films," *Appl. Phys. Lett.*, vol. 69, no. 14, pp. 2027–2029, Sep. 1996, doi: 10.1063/1.116868.

[8] D. Gall, "The search for the most conductive metal for narrow interconnect lines," *J. Appl. Phys.*, vol. 127, Feb. 2020, Art. no. 050901, doi: 10.1063/1.5133671.

[9] B.-S. Lee et al., "Development of electrodeposited $IrO_2$ electrodes as anodes in polymer electrolyte membrane water electrolysis," *Appl. Catalysis B, Environ.*, vol. 179, pp. 285–291, 2015, doi: 10.1016/j.apcatb.2015.05.027.

[10] C. D. Wagner, A. V. Naumkin, A. Kraut-Vass, J. W. Allison, C. J. Powell, and J. R. Rumble, *NIST Standard Reference Database 20, Version 3.4*, 2003. [Online]. Available: http:/srdata.nist.gov/xps/

[11] W.-P. Wu and Z.-F. Chen, "Iridium coating: Processes, properties and application," *Johnson Matthey Technol. Rev.*, vol. 61, no. 2, pp. 93–110, 2017, doi: 10.1595/205651317X695064.

[12] H. F. Ragaie, "Grain boundary diffusion in columnar structure polycrystalline materials," *Electron. Lett.*, vol. 19, pp. 294–295, 1983.

[13] E. Navickas et al., "Fast oxygen exchange and diffusion kinetics of grain boundaries in Sr-doped $LaMnO_3$ thin films," *Phys. Chem. Chem. Phys.*, vol. 17, pp. 7659–7669, 2015, doi: 10.1039/C4CP05421K.

[14] Z. Pavlovic, C. Ranjan, Q. Gao, M. van Gastel, and R. Schlögl, "Probing the structure of a water-oxidizing anodic iridium oxide catalyst using Raman spectroscopy," *ACS Catalysis*, vol. 6, pp. 8098–8105, 2016, doi: 10.1021/acscatal.6b02343.

[15] A. V. Korotcov, Y. Huang, K. Tiong, and D. Tsai, "Raman scattering characterization of well-aligned $RuO_2$ and $IrO_2$ nanocrystals," *J. Raman Spectrosc.*, vol. 38, pp. 737–749, 2007, doi: 10.1002/jrs.1655.

[16] F. Huang et al., "Insight into factors influencing thermal oxidation of iridium oxide electrode: Thermostatic post-treatment temperature," *J. Electrochem. Soc.*, vol. 169, 2022, Art. no. 037530, doi: 10.1149/1945-7111/ac5f20.

[17] A. Avila-García, G. Romero-Paredes, and R. Peña-Sierra, "Iridium oxide films obtained by thermo-chemical transformation," in *Proc. 7th Int. Conf. Elect. Eng. Comput. Sci. Autom. Control*, 2010, pp. 537–540, doi: 10.1109/ICEEE.2010.5608590.

[18] H. Guan et al., "Amorphous iridium oxide nanoparticle films prepared by low temperature annealing and plasma treatment as highly efficient oxygen evolution electrocatalysts," *Chem. Lett.*, vol. 49, pp. 705–708, 2020, doi: 10.1246/cl.200133.